Nonsinusoidal gaits for unsteady propulsion

T. Van Buren,[1,*] D. Floryan,[1] D. Quinn,[2] and A. J. Smits[1]
[1]*Mechanical and Aerospace Engineering, Princeton University, Princeton, New Jersey 08544, USA*
[2]*Mechanical and Aerospace Engineering, University of Virginia, Charlottesville, Virginia 22904, USA*
(Received 27 January 2017; published 17 May 2017; corrected 22 May 2017)

The impact of wave-form shape on the wake and propulsive performance of a pitching and heaving two-dimensional foil is explored experimentally. Jacobi elliptic functions are used to define wave-form shapes that are approximately triangular, sinusoidal, or square. The triangular-like and sinusoidal waves produce qualitatively similar wakes, with a typical reverse von Kármán vortex street structure leading to a jetlike wake in the mean. Square-like motions produce very different results, with a vortex pair shed every half cycle, leading to a mean wake with two distinct off-center jets, and a significant change in the thrust production, yielding up to four times more thrust for a given Strouhal number. Performance curves indicate that to swim most efficiently sinusoidal motions are best, whereas the square-like motions lead to higher speeds. A scaling analysis indicates that the peak lateral velocity appears to be the dominant parameter in characterizing the performance of the nonsinusoidal motions.

DOI: 10.1103/PhysRevFluids.2.053101

I. INTRODUCTION

Certain aquatic animals, for example, dolphins, sailfish, and tuna, are capable of extraordinary swimming performance, with the ability to swim fast and efficiently over long distances. This observation has prompted many researchers to study the propulsive characteristics of fish to help design new aquatic propulsion technologies [1–3]. With very few exceptions, these investigations have only considered sinusoidal motions [4–8], although fish and swimming mammals may use different actuation wave forms while swimming near a boundary or a water surface, during maneuvering, or when performing burst and coast-type swimming [9–12]. The experiments that have been performed on unsteady foils have shown that deviations from sinusoidal actuation changes the structure of the wake [13] and affects the propulsive performance [14,15], results that were confirmed by numerical study [16]. Despite this work, it is clear that our understanding of the effects of wave-form shape on swimming performance is only rudimentary. Here, we explore a simple family of wave-form shapes chosen because of their ease of implementation. Although these specific wave-form shapes may not have been observed in nature, we are not bound by the limits of biology and there is much to learn by moving beyond them.

To understand these effects better, we consider the performance of a two-dimensional foil undergoing pitching (twisting about the leading edge) and heaving (lateral foil translation) motions with nonsinusoidal wave forms. In unsteady propulsion, there are two main contributions to the forces acting on the foil: quasisteady lift-based forces [17] and added mass forces due to fluid acceleration [18]. Changing the actuation wave form alters the relative contributions of these forces. For example, a square wavelike motion has a larger peak acceleration than a sinusoidal motion with the same frequency and amplitude, and thus it experiences a relatively larger added-mass force contribution. We find that the actuation wave-form shape can have a substantial effect on the thrust and efficiency over a large range of frequencies and amplitudes and a dramatic effect on the vortex structure in the wake of the foil.

*tburen@princeton.edu

 ©2017 American Physical Society

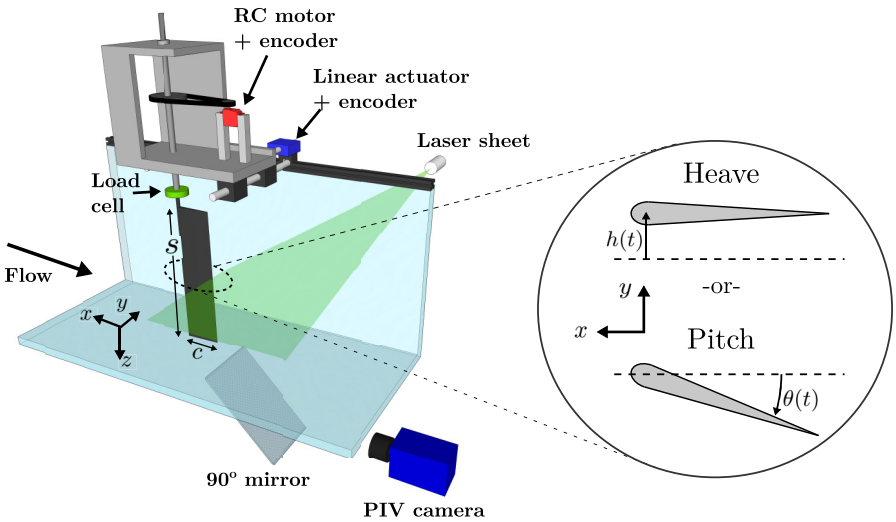

FIG. 1. Experimental setup.

II. EXPERIMENTAL SETUP

Experiments were conducted in a water channel on a pitching or heaving foil, as shown in Fig. 1. The water channel is a free-surface recirculating facility with a 0.46-m-wide, 0.3-m-deep, and 2.44-m-long test section. Surface waves were minimized through baffles equipped on the top surface. The free-stream velocity U was fixed at 60 mm/s with a maximum turbulence intensity of 0.8%.

A nominally two-dimensional teardrop foil was used, with a chord of $c = 80$ mm, maximum thickness 8 mm, and span $s = 279$ mm, resulting in a chord-based Reynolds number of $\mathrm{Re}_c = 4870$. The foil extended from the bottom of the tunnel to the surface baffles, with gaps of less than 5 mm. Heaving motions were driven by a linear actuator (LinMot PS01-23x80F-HP-R) on air bearings (NewWay S301901), and pitching motions were controlled through an RC motor (Hitec HS-8370TH). Both motion types were monitored via encoders.

Jacobi elliptic functions define the motion wave form [19], resulting in a continuous space of wave forms controlled by a single parameter, the elliptic modulus κ, spanning from approximate triangular waves ($\kappa = -1$), to sinusoidal waves ($\kappa = 0$), to approximate square waves ($\kappa \to 1$). To avoid motions with unreasonably high accelerations, we varied κ from -0.99 to 0.99. The wave-form shapes are not perfectly triangular and square, and will be hereby referred to as triangular-like and square-like motions. See Fig. 2 for examples of wave-form shapes (colored circles will be used for explanation in Sec. III).

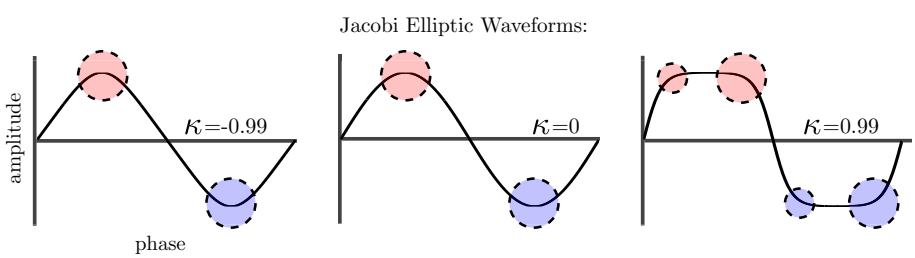

FIG. 2. Jacobi elliptic functions produce varying actuation wave-form shape based on the elliptic modulus, κ. Colored circles represent points of vortex production in the cycle based on particle image velocimetry (PIV) measurements, and smaller circles correspond to secondary vortices (see Sec. V).

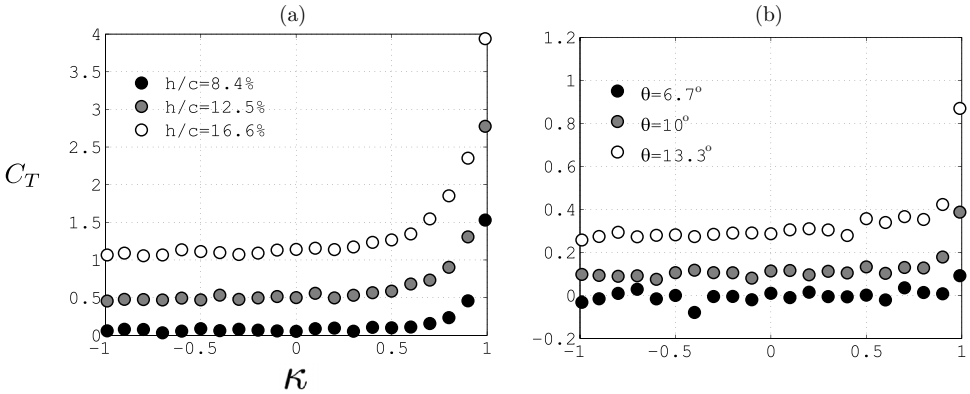

FIG. 3. Thrust coefficient as a function of elliptic modulus. (a) Heaving at reduced frequency $f^* = 1.2$; (b) pitching at $f^* = 0.87$. The wave forms range from triangular-like ($\kappa = -0.99$), to sinusoidal ($\kappa = 0$), to square-like ($\kappa = +0.99$).

The thrust, power, and efficiency were measured using a six-component force-torque sensor (ATI Mini40), with force and torque resolutions of 5×10^{-3} N and 1.25×10^{-4} N m, respectively. The heave and pitch amplitudes ranged from $h_0 = 5$ to 15 mm every 2 mm and $\theta_0 = 3^\circ$ to 15° every 2°. The actuation frequency f was varied such that the Strouhal number $\mathrm{St} = 2fA/U$ ranged from 0.05 to 0.4 in increments of 0.025, with a maximum frequency of 2 Hz. Here, A is the trailing edge amplitude of motion. Square-like motions exceeding frequencies of 1.2 Hz were not investigated because they excited an undesirable structural resonance. Each trial consisted of 30 cycles, and the data were averaged over the middle 20 cycles. Each trial was repeated a minimum of 5 times to ensure repeatability and reduce uncertainty.

Flow velocities were measured using two-component particle image velocimetry (PIV). Neutrally buoyant silver-coated hollow ceramic spheres (Potter Industries Inc., Conduct-O-Fil AGSL150 TRD) were used to seed the flow, illuminated on the midspan using a CW argon-ion laser (Spectra Physics 2020). An 8-bit monochrome CCD camera (MotionXtra HG-LE) with 1128×752 resolution was used to acquire images at 25 Hz. A minimum of 10 actuation periods were sampled for phase averaging. Three PIV windows were taken and stitched together to encompass the entire flow around the foil and 1.5 chords downstream in the wake. Sequential images were processed using commercial DaVis software using spatial correlation interrogation window sizes of 64×64 and twice at 32×32 with 50% overlap. The full vector field contained a grid size of 119×47 velocity vectors. Average and instantaneous velocity errors are estimated to be 2.7% and 1–5%, respectively [20].

III. PROPULSIVE PERFORMANCE

Performance measurements range from $\mathrm{St} = 0.05$ to 0.4 every 0.025 with multiple amplitudes and frequencies. The thrust coefficient, power coefficient, and efficiency are defined according to

$$C_T = \frac{F_x}{\frac{1}{2}\rho U^2 sc}, \quad C_P = \frac{F_y\dot{h} + M_z\dot{\theta}}{\frac{1}{2}\rho U^3 sc}, \quad \eta = \frac{C_T}{C_P}, \tag{1}$$

where F_x and F_y are the streamwise and cross-stream forces acting on the foil, M_z is the spanwise moment, and ρ is the fluid density.

The effect of changing the elliptic modulus on the thrust coefficient is shown in Fig. 3, where $f^* = fc/U$ is the reduced frequency. We see that the thrust for both heaving and pitching motions is essentially constant for most values of κ, but for more square-like wave-forms motions the thrust increases dramatically, with an earlier onset for heave ($\kappa = 0.5$) than for pitch ($\kappa = 0.99$).

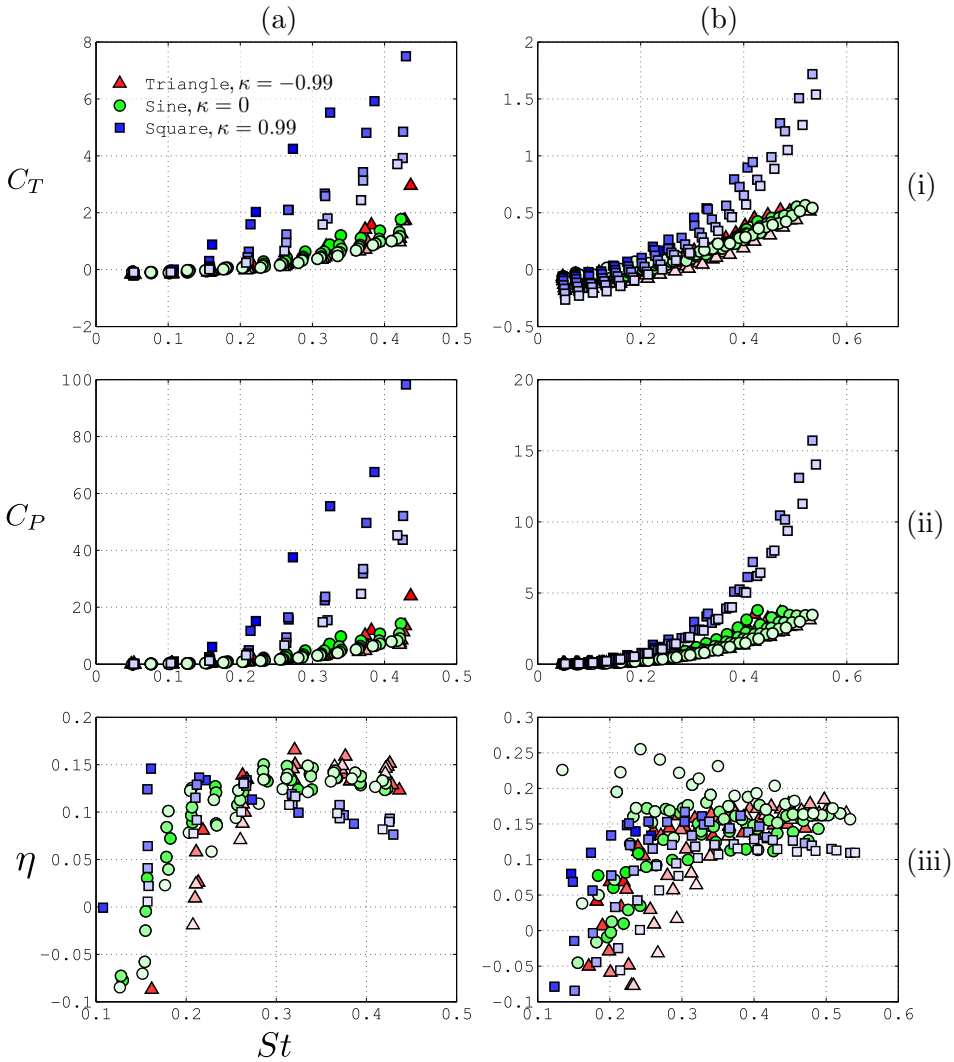

FIG. 4. Performance as a function of Strouhal number for (a) heave and (b) pitch. Subfigures show (i) thrust coefficient, (ii) power coefficient, and (iii) efficiency. Symbol color identifies the wave-form shape, and tone represents amplitude of motion ranging from low (dark) to high (light). For heave, $h/c = 6.25\%$ to 18.75% every 2.5%. For pitch, $\theta = 3^\circ$ to 15° every 2°.

The changes in thrust and power with wave-form shape are clearly seen in Fig. 4 across a range of Strouhal numbers. For both heave and pitch, the thrust and power increase monotonically with Strouhal number, and square-like motions exhibit higher thrust and power than the triangular-like and sinusoidal motions. Also, thrust and power coefficients for heave are typically considerably larger than for pitch, with similar efficiencies. This corroborates Fig. 3.

For pitching motions, the effect of viscous drag is to reduce the thrust by an almost constant offset (see Floryan *et al.* [21]). This effect is more pronounced for the square-like motions [most visible in Fig. 4(b)(i) at low Strouhal numbers] because the foil spends more time near its maximum pitch angle, though similar trends exist in the other motion types. For heaving motions, a similar effect of increasing drag with increasing amplitude of motion is observed, but the drag does not produce a simple offset, and the larger amplitude of the thrust obscures the trend somewhat.

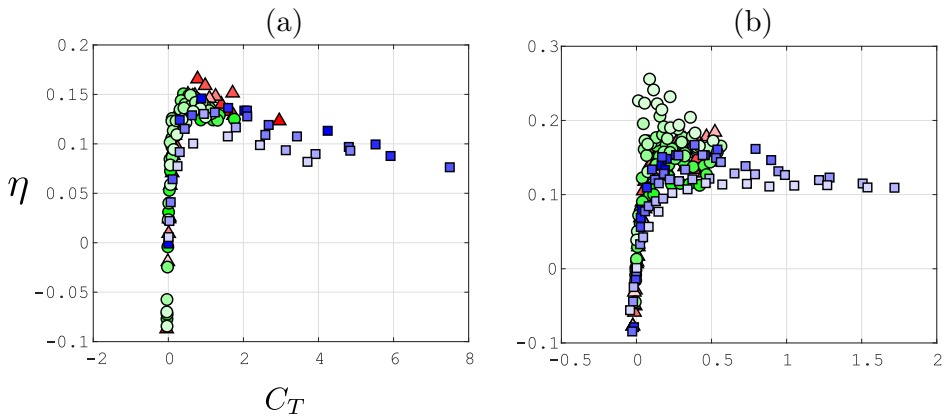

FIG. 5. Efficiency vs thrust coefficient for (a) heave and (b) pitch. Symbols and colors as in Fig. 4.

For efficiency, the effects of wave-form shape are more subtle. In heave, the peak efficiency does not appear to be affected very much by wave-form shape, although the Strouhal number corresponding to the peak efficiency occurs at a much lower value for the square-like motion, accompanied by a much more rapid drop-off at higher Strouhal numbers. In pitch, there are slightly higher peak efficiencies in the sinusoidal motions, but only at the lowest amplitude. Generally, the location of peak efficiency occurs at lower Strouhal numbers for higher elliptic moduli.

Perhaps a more practical way to view efficiency is to show it as a function of thrust, as given in Fig. 5. For heave, the effects of wave-form shape are rather minor (within the range of amplitudes studied here), but for pitch increasing κ tends to decrease the efficiency at a given thrust, and the highest peak efficiency is achieved with sinusoidal motions. We see that actuation wave form can be used to regulate thrust-efficiency tradeoffs during locomotion, for a given frequency and amplitude.

IV. PERFORMANCE SCALING

Floryan *et al.* [21] found that for sinusoidal motions of a two-dimensional foil similar to that used in the present study, the thrust and power coefficients scaled with both Strouhal number St and reduced frequency f^* according to

$$C_T = c_1\,\mathrm{St}^2 + c_2\,\mathrm{St}^2\,f^*U^* - C_{D_h}, \quad C_P = c_3\,\mathrm{St}^2 + c_4\,\mathrm{St}^2\,f^* + c_5\,\mathrm{St}^2\,f^*U^*$$

for heaving motions, and

$$C_T = c_6\,\mathrm{St}^2 - C_{D_p}, \quad C_P = c_7\,\mathrm{St}^2 + c_8\,St^2\,f^*$$

for pitching motions. Here C_{D_h} and C_{D_p} are the drag coefficients for each motion, and $c_1 - c_8$ are empirical constants.

For sinusoidal motions, the trailing-edge position, velocity, and acceleration (at a given phase) are completely defined by the amplitude of the motion A and the actuation frequency f. For motions that follow Jacobi elliptic functions, the position, velocity, and acceleration will also depend on the elliptic modulus κ. Figure 6 presents the peak velocity, $\dot{a}$, and acceleration, $\ddot{a}$, of the trailing edge for motion types ranging from $-0.99 \leqslant \kappa \leqslant 0.99$, normalized by their respective sinusoidal values. The peak velocity and acceleration behave similarly, in that they are relatively unchanged at lower elliptic moduli but increase sharply as κ approaches 1. The variation of thrust with κ (see Fig. 3) suggests that the thrust may scale with wave-form peak velocity, especially for heaving motions.

To explore this possibility, we introduce a trailing edge peak velocity scale, $\dot{a}^* = \dot{a}/\dot{a}_{\kappa=0}$, which only varies with elliptic modulus. We find that P_2, a quadratic function of $\dot{a}^*$, can be used to scale

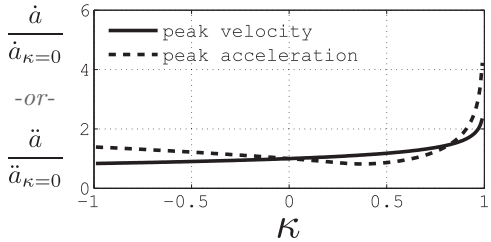

FIG. 6. Peak velocity and acceleration as it varies with elliptic modulus.

the performance, where

$$P_2 = b_1\,\dot{a}^* + b_2\,\dot{a}^{*2} \tag{2}$$

and b_1 and b_2 are constants. Figure 7 shows that the thrust and power coefficients scaled with P_2 are nearly constant across the entire range of κ, and the highly nonlinear variation with elliptic modulus is almost entirely removed.

When we combine the scaling of Floryan *et al.* [21] with the peak velocity scaling parameter, P_2 (without changing the empirical constants $c_1 - c_8$ from the original analysis), we obtain an encouraging collapse of the thrust and power coefficients for a large range of motion parameters, as shown in Fig. 8. It appears that the peak velocity scale, $\dot{a}^*$, fully defines nonsinusoidal pitching and heaving performance, at least for the range of parameters investigated here.

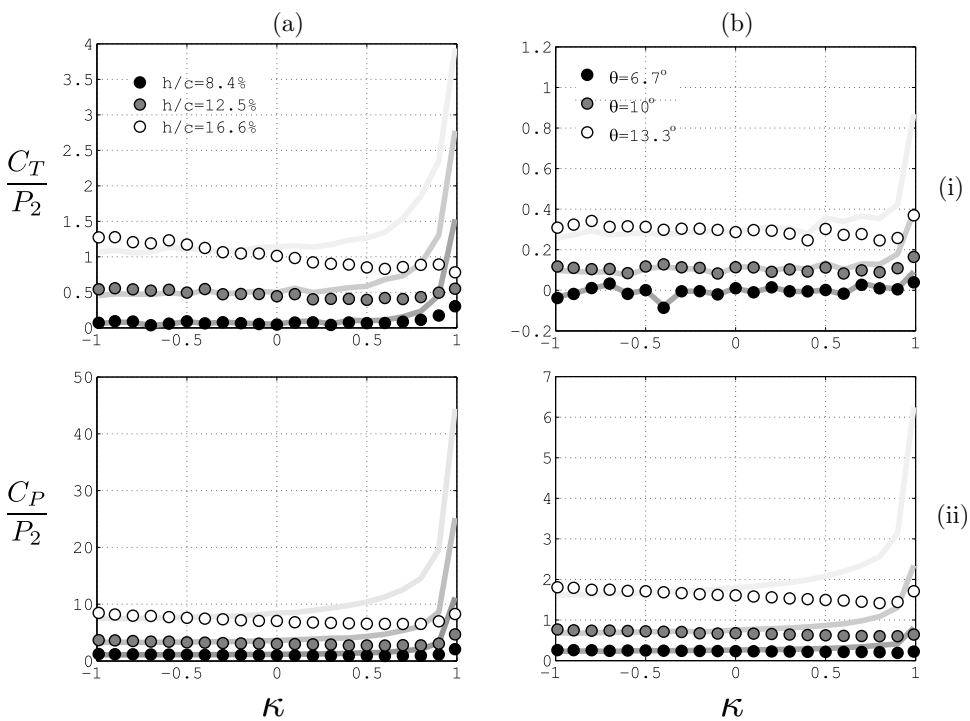

FIG. 7. (i) Thrust and (ii) power coefficients scaled by a quadratic function of the peak waveform velocity [Eq. (2)] as a function of elliptic modulus. (a) Heaving at reduced frequency $f^* = 1.2$; (b) pitching at $f^* = 0.87$. Faint lines represent unscaled data, as in Fig. 3. Constants: (a) (i) $b_1 = 0.4$, $b_2 = 0.8$; (a) (ii) $b_1 = 0.4$, $b_2 = 0.8$; (b) (i) $b_1 = 1$, $b_2 = 0$; (b)(ii) $b_1 = 0.8$, $b_2 = 0.3$.

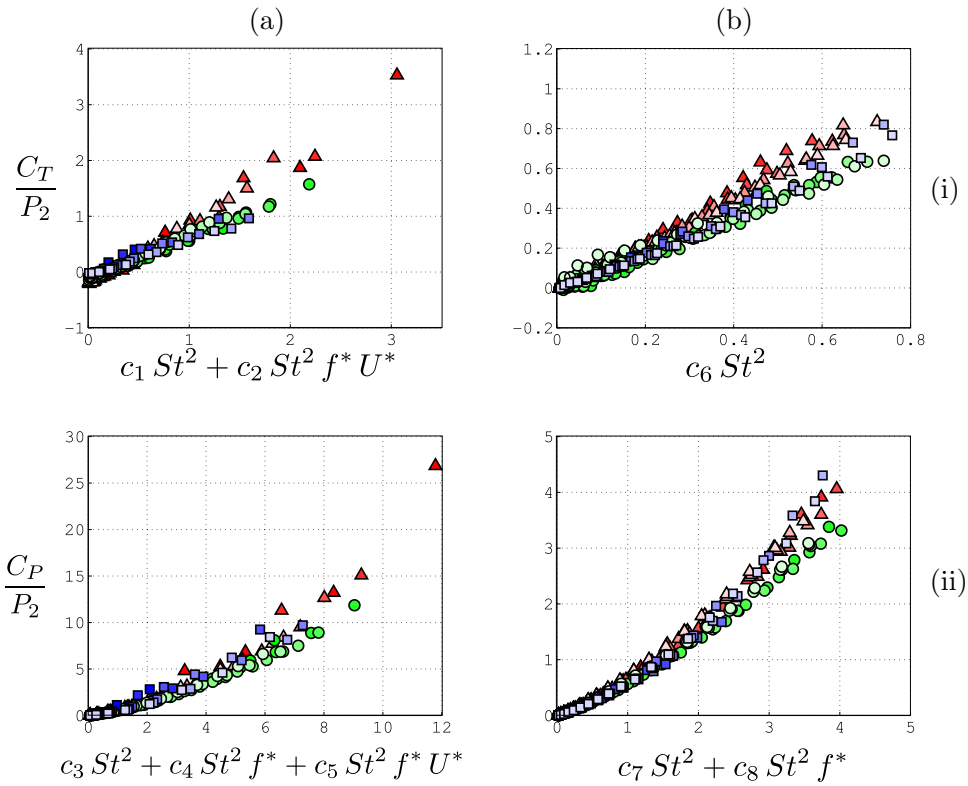

FIG. 8. The foil (i) thrust and (ii) power modified by the lateral velocity scale plotted against the scaling proposed by Floryan *et al.* [21] for (a) heave and (b) pitch. Symbols and tones as in Fig. 4.

V. WAKE EVOLUTION

To investigate the effects of wave-form shape on the vortex shedding from the foil, and the evolution of the wake, PIV measurements were made at Strouhal numbers of St = 0.2, 0.3, and 0.4, where the Strouhal number was varied by changing the amplitude while keeping the frequency fixed. We only present results for $St = 0.4$ since the flow fields at the lower Strouhal numbers were qualitatively similar.

Figure 9 shows the phase-averaged vorticity field for the heaving foil with triangular-like, sinusoidal, and square-like motions. The sinusoidal and triangular-like motion types have similar wake structures, characterized by a reverse von Kármán vortex street that is typical of propulsors in the thrust state. The structure of the square-like motion is quite different, however, with vortex pairs released from the trailing edge instead of single vortices. This result in not surprising in that triangular-like and sinusoidal motions change direction smoothly, thus producing a single vortex per cycle, whereas a square-like motion stops rapidly, remains stationary for some part of the cycle, and then movies rapidly in the opposite direction, thus producing two vortices of opposite sign per cycle. This is shown schematically in Fig. 2. These vortex pairs have higher mutually induced velocities, causing them to move downstream faster than is the case for the sinusoidal and triangular-like motions, as indicated by the lines connecting the four phases in Fig. 9.

The pitching foil behavior, shown in Fig. 10, is qualitatively similar. The square-like motion produces a vortex pair, but the secondary vortex is weaker in pitch than in heave. Also, the primary trailing edge vortices in pitch are stronger for the square-like motions, whereas in heave there was no noticeable difference in vortex strength between the three motion types. This may be explained

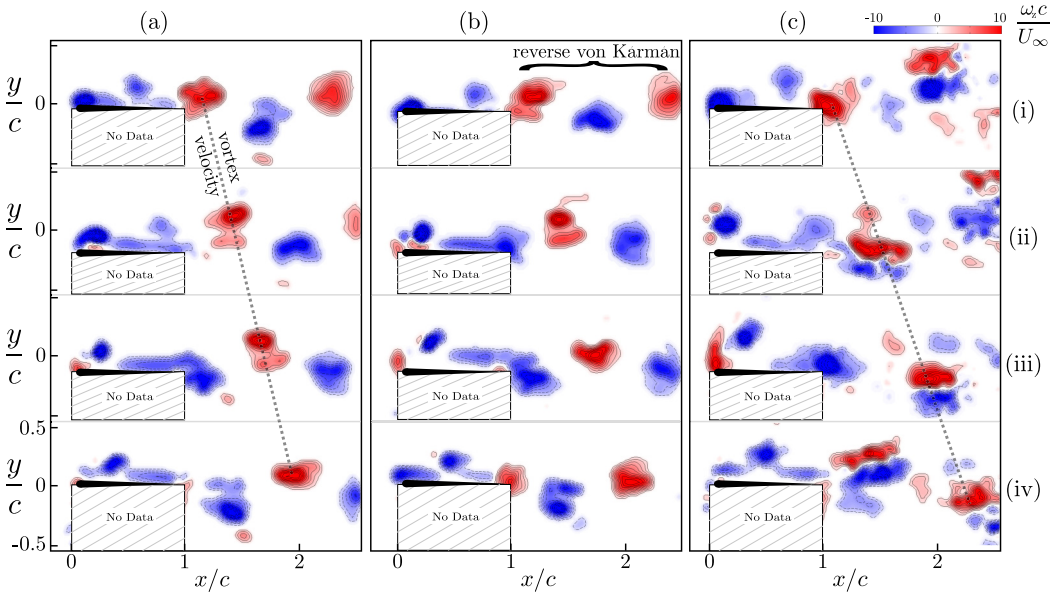

FIG. 9. Heaving motions, phase-averaged spanwise vorticity, $h/c = 12.5\%$, $St = 0.4$. Waveform types: (a) triangular-like $\kappa = -0.99$; (b) sinusoidal $\kappa = 0$; (c) square-like $\kappa = 0.99$. Phases: (i) $\phi = 0^\circ$; (ii) 90°; (iii) 180°; (iv) 270°.

by noting that in pitch the thrust is governed primarily by added mass [21], and a square-like motion produces higher accelerations than sinusoidal and triangular-like motions, directly impacting vortex strength. In contrast, in heave the thrust is mostly lift based, so the relationship between foil acceleration and shed vorticity is more complex.

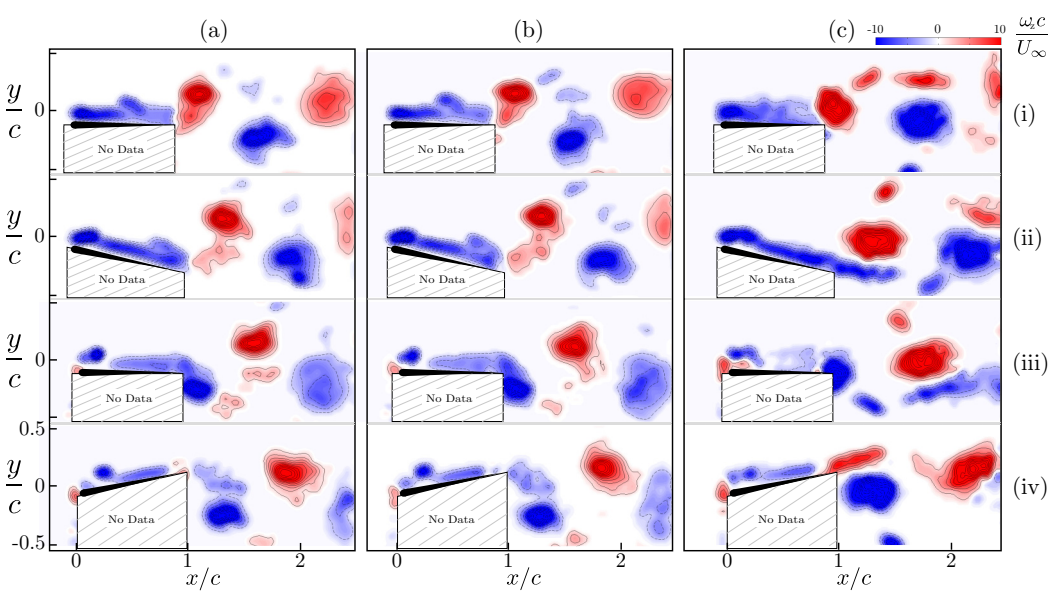

FIG. 10. Pitching motions, phase-averaged spanwise vorticity, $\theta = 14.5^\circ$, St $= 0.4$. Wave-form types: (a) triangular-like $\kappa = -0.99$; (b) sinusoidal $\kappa = 0$; (c) square-like $\kappa = 0.99$. Phases: (i) $\phi = 0^\circ$, (ii) 90°, (iii) 180°, (iv) 270°.

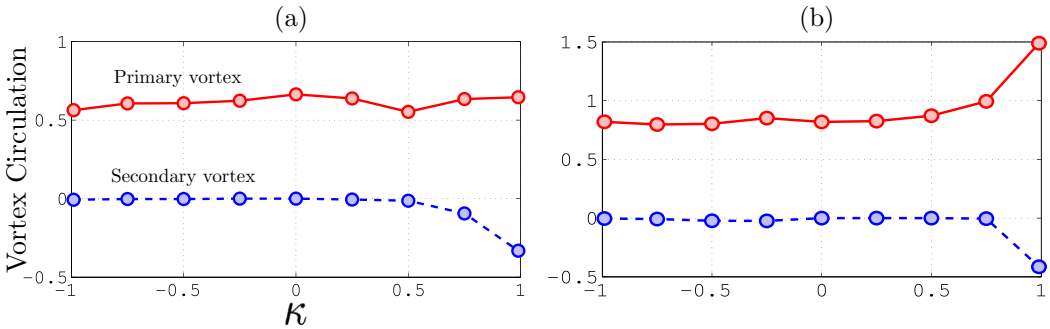

FIG. 11. Primary and secondary vortex circulation as a function of elliptic modulus for (a) heaving and (b) pitching motions at St = 0.4.

The strengths of the primary and secondary vortex are shown in Fig. 11 as a function of the elliptic modulus. Here, we track the cycle when the primary vortex is positive and the secondary vortex is negative and we compute the circulation from within a boundary containing only that vortex. In heave, the primary vortex strength is relatively constant for all wave-form shapes, whereas in pitch the primary vortex strength increases as the motion becomes more square-like. The secondary vortex only begins to appear at $\kappa > 0.5$ for heave and $\kappa = 0.99$ for pitch. In square-like motions, the primary vortex is twice as strong as the secondary in heave, and in pitch the primary vortex is three times stronger. The presence of the secondary vortex directly correlates to the large increase in thrust shown in Fig. 3 at the corresponding values of κ.

The secondary vortex significantly alters the trajectory of the primary vortex, as seen in Fig. 12. Here the trajectory follows the approximate peak vorticity of the primary vortex. For triangular-like and sinusoidal motion types, for $-0.99 \leqslant \kappa \leqslant 0$, the primary vortex remains on the side in which it was formed, which leads to the reverse von Kármán vortex street structure. As the motions become more square-like ($\kappa > 0.5$), the primary vortex moves to the opposite side of the foil as it convects downstream under the action of the velocity induced by the secondary vortex. In heaving square-like motions where the strength of the primary and secondary vortices are similar, the vortex pair rapidly crosses to the side of the foil opposite to the one where it was formed, and then follows the free-stream direction. In pitch, where the strength of the primary vortex is about three times larger than that of the secondary vortex, the primary vortex first heads towards the opposite side of the foil before

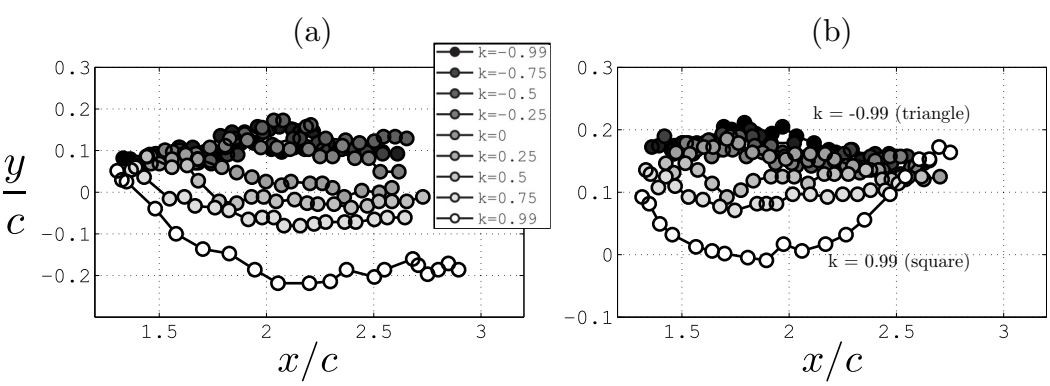

FIG. 12. Primary vortex trajectory in the streamwise plane for different values of κ. (a) Heaving and (b) pitching motions at St = 0.4.

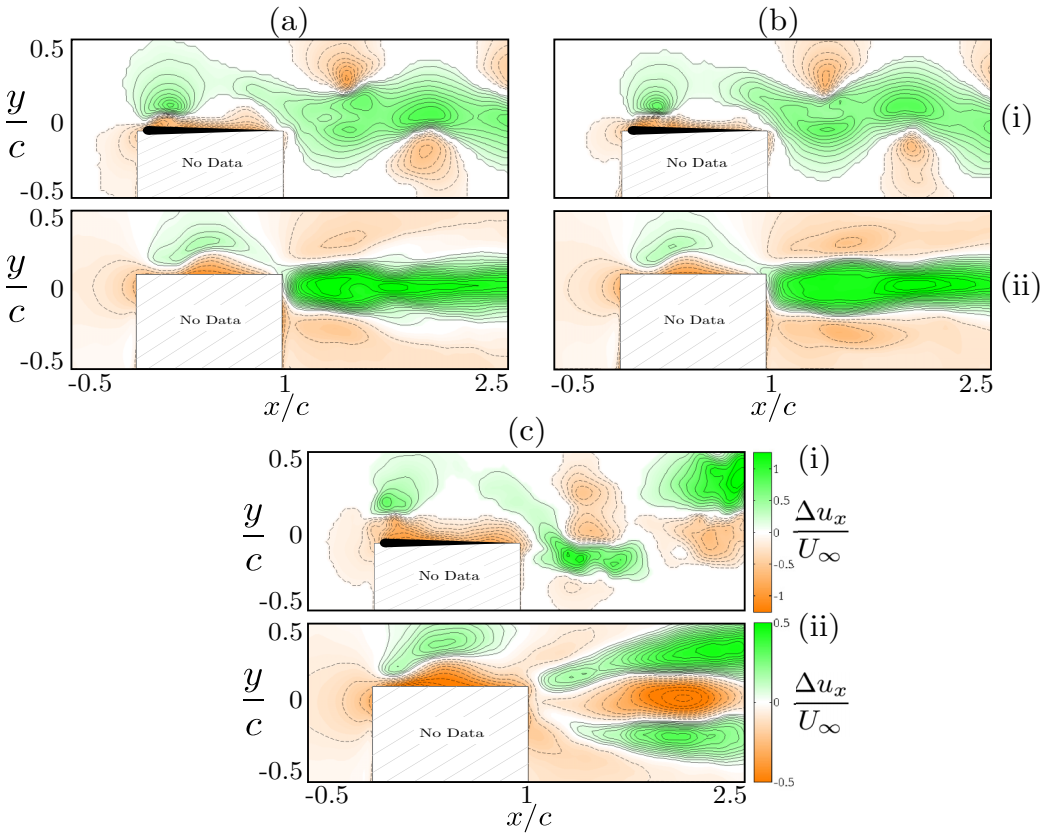

FIG. 13. Heaving foil. (i) Phase- and (ii) time-averaged Δu_x ($h/c = 12.5\%$, $\mathrm{St} = 0.4$). Wave form: (a) triangular-like $\kappa = -0.99$, (b) sinusoidal $\kappa = 0$, (c) square-like $\kappa = 0.99$.

curving back to the original side. This happens because the weaker secondary vortex orbits the primary vortex, thereby rotating the direction of its induced velocity.

Next, we explore the impact the unsteady foil has on the surrounding velocity field. Figure 13 depicts the phase- and time-averaged change in streamwise velocity, relative to the free-stream, for the heaving cases shown in Fig. 9(i). Instantaneously, the triangular-like and sinusoidal motions produce a wavy region of accelerated fluid near the centerline corresponding to the region contained within the vortex street, with pockets of decelerated flow appearing externally. In the time-averaged field, this results in a jetlike wake on the centerline. Square-like motions produce pockets of higher and lower velocity that correspond to the vortex pairs, yielding a time-averaged pair of jets off the centerline. The velocity fields produced by pitching motions are broadly similar, as shown in Fig. 14, but the square-like motions do not create a dual jet, only a single wider single jet, because in these cases the secondary vortex is not strong enough to separate the vortex pair trajectories and produce two distinct jets in the time average.

To compare the entire range of wave-form shapes tested, the time-averaged velocity profile of the heaving and pitching panels at $x/c = 1$ is shown in Fig. 15. In heave, the wake transitions from a typical jet in triangular-like and sinusoidal motions to a dual jet at $\kappa = 0.5$. This directly corresponds to the generation of the secondary vortex discussed in Fig. 11. For pitching motions, the wake is jetlike for the entire range of wave-form shapes, though the wake for the square-like motions is stronger and more spread out than the triangular-like and sinusoidal motions.

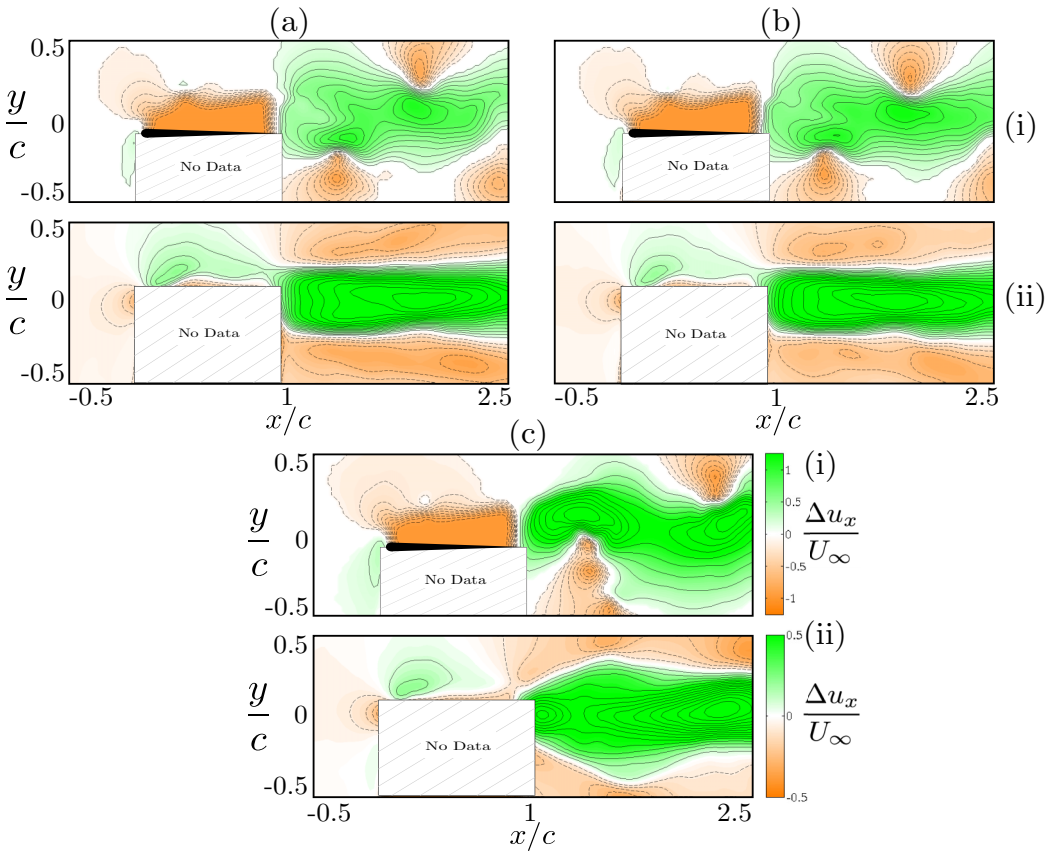

FIG. 14. Pitching foil. (i) Phase- and (ii) time-averaged Δu_x ($\theta = 14.5°$, St $= 0.4$). Wave form: (a) triangular-like $\kappa = -0.99$, (b) sinusoidal $\kappa = 0$, (c) square-like $\kappa = 0.99$.

VI. CONCLUSIONS

The effects of oscillatory motion shape of a two-dimensional teardrop foil were studied experimentally in an effort to better understand unsteady fish propulsion and discover new techniques for improving propulsive performance. The motion types were defined by Jacobi elliptic functions, which span from approximated triangular-like, through sinusoidal, to square-like wave forms with a single parameter, the elliptic modulus.

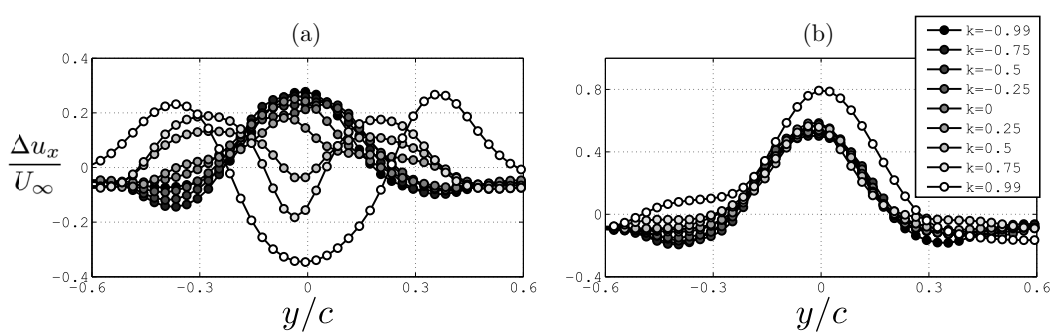

FIG. 15. Velocity profiles at $x/c = 1$ for different values of κ. (a) Heave and (b) pitch at St $= 0.4$.

The wave-form shape had a dramatic impact on the vortex structure produced in the wake of the foil. The rapid start and stop of square-like wave type motions produces vortex pairs instead of the typical vortex street, resulting in a dual-jet velocity wake. These effects are more pronounced in heave than in pitch, though similar trends were found in both and across all Strouhal numbers studied ($\mathrm{St} = 0.2$, 0.3, and 0.4). Triangular-like and sinusoidal motions showed more typical behavior, with a reverse von Kármán vortex street and a single jet wake.

This formation of vortex pairs, and the corresponding time-averaged dual-jet wake associated with square-like motions, was closely correlated to large increases in the thrust, producing up to 4 times higher forces than the motions with a typical wake. In heave, the peak efficiency was not impacted by the wave-form shape, whereas in pitch sinusoidal motions had the peak efficiency. It was found that the performance depended primarily on the peak lateral velocity of the trailing edge. By using a quadratic form of the lateral velocity scale combined with the scaling of sinusoidal motions proposed in Floryan *et al.* [21], the performance data could be collapsed for heaving and pitching motions for all wave-form shapes investigated here.

Animals and vehicles could thus use nonsinusoidal motions to increase thrust, efficiency, or swimming speed, depending on the situation. A square wave, for example, could be used to accelerate quickly, whereas a sinusoid could be used for efficient cruise. This concept is consistent with the diversity of motion types seen in biological swimmers, and it suggests new strategies for effective motor control in swimming robots.

ACKNOWLEDGMENT

This work was supported by ONR Grant N00014-14-1-0533 (Program Manager Robert Brizzolara).

---

[1] J. O. Dabiri, Optimal vortex formation as a unifying principle in biological propulsion, Annu. Rev. Fluid Mech. **41**, 17 (2009).

[2] M. S. Triantafyllou, G. S. Triantafyllou, and D. K. P. Yue, Hydrodynamics of fishlike swimming, Annu. Rev. Fluid Mech. **32**, 33 (2000).

[3] T. Y. Wu, Fish swimming and bird/insect flight, Annu. Rev. Fluid Mech. **43**, 25 (2011).

[4] J. M. Anderson, K. Streitlien, D. S. Barrett, and M. S. Triantafyllou, Oscillating foils of high propulsive efficiency, J. Fluid Mech. **360**, 41 (1998).

[5] G. C. Lewin and H. Haj-Hariri, Modelling thrust generation of a two-dimensional heaving airfoil in a viscous flow, J. Fluid Mech. **492**, 339 (2003).

[6] M. J. Lighthill, Aquatic animal propulsion of high hydromechanical efficiency, J. Fluid Mech. **44**, 265 (1970).

[7] D. B. Quinn, G. V. Lauder, and A. J. Smits, Scaling the propulsive performance of heaving flexible panels, J. Fluid Mech. **738**, 250 (2014).

[8] Z. J. Wang, Vortex shedding and frequency selection in flapping flight, J. Fluid Mech. **410**, 323 (2000).

[9] F. E. Fish, J. F. Fegely, and C. J. Xanthopoulos, Burst-and-coast swimming in schooling fish (*Notemigonus crysoleucas*) with implications for energy economy, Comp. Biochem. Physiol. Part A: Physiol. **100**, 633 (1991).

[10] G. V. Lauder, Locomotion, in *The Physiology of Fishes*, 3rd ed., edited by D. H. Evans and J. B. Claiborne (CRC Press, Boca Raton, FL, 2005), pp. 3–46.

[11] G. V. Lauder, Fish locomotion: Recent advances and new directions, Annu. Rev. Marine Sci. **7**, 521 (2015).

[12] J. J. Videler and D. Weihs, Energetic advantages of burst-and-coast swimming of fish at high speeds, J. Exp. Biol. **97**, 169 (1982).

[13] M. M. Koochesfahani, Vortical patterns in the wake of an oscillating airfoil, AIAA J. **27**, 1200 (1989).

[14] M. Kaya and I. H. Tuncer, Nonsinusoidal path optimization of a flapping airfoil, AIAA J. **45**, 2075 (2007).
[15] D. A. Read, F. S. Hover, and M. S. Triantafyllou, Forces on oscillating foils for propulsion and maneuvering, J. Fluids Struct. **17**, 163 (2003).
[16] K. Lu, Y. H. Xie, and D. Zhang, Numerical study of large amplitude, nonsinusoidal motion and camber effects on pitching airfoil propulsion, J. Fluids Struct. **36**, 184 (2013).
[17] J. D. Anderson Jr., *Fundamentals of Aerodynamics* (Tata McGraw-Hill Education, New York, 2010).
[18] L. I. Sedov, *Two-Dimensional Problems in Hydrodynamics and Aerodynamics* (Interscience, New York, 1965).
[19] M. Abramowitz and I. A. Stegun, Jacobian elliptic functions and theta functions, in *Handbook of Mathematical Functions: With Formulas, Graphs, and Mathematical Tables* (Dover Publications, New York, 1972), Chap. 16.
[20] A. Sciacchitano, B. Wieneke, and F. Scarano, PIV uncertainty quantification by image matching, Meas. Sci. Technol. **24**, 045302 (2013).
[21] D. Floryan, T. Van Buren, C. W. Rowley, and A. J. Smits, Scaling the propulsive performance of heaving and pitching foils, J. Fluid Mech. (to be published), arXiv:1704.07478.